

Effective Polarization Filtering Techniques for Ground Penetrating Radar Applications

Sebastian G. Wirth and Ivor L. Morrow

Cranfield University, Electromagnetic Systems Engineering Group, Oxfordshire, SN6 8LA, UK.

Email: sebastian.wirth@cranfield.ac.uk; i.l.morrow@cranfield.ac.uk

Abstract—The effect of different decomposition techniques on the imaging and detection accuracy for polarimetric surface penetrating radar data is studied. We derive the general expressions for coherent polarimetric decomposition using the Stokes parameters and model based polarimetric decomposition using the Yamaguchi technique. These techniques are applied to multi-frequency (0.4-4.8GHz) full polarimetric near-field radar measurements of scattering from surface laid calibration objects and shallow buried landmine types and show in detail how the decomposition results provide effective surface and sub-surface clutter reduction and guide the interpretation of scattering from subsurface objects. Data processing methods assume cross-polar symmetry and a novel bistatic calibration procedure was developed to enforce this condition. The Yamaguchi polarimetric decomposition provides significant clutter reduction and image contrast with some loss in signal power; while Stokes parameters also provide imagery localising targets, complementary information on the scattering mechanism is also obtained. Finally a third novel polarimetric filter was formulated based on differential interferometric polarimetric decomposition. The three combined techniques contribute to a significant improvement of subsurface radar performance and detection image contrast.

I. INTRODUCTION

Ground penetrating radar (GPR) is increasingly being used for landmine detection [1],[2]. In contrast to metal detecting, GPR can be used for detection of low-metal content or non-metal content targets. Subsurface radar still suffers from two typical problems, a strong clutter response from the surface and high signal to clutter levels in the underground [3],[4],[5]. This paper addresses these problems through the use of a novel near-field full-polarimetric (0.4-4.8 GHz) SFCW GPR system that measures the polarimetric microwave backscatter response and synthesises an equivalent complex clutter scattering matrix that suppresses subsurface clutter in the co-polar and cross-polar channels [6],[7]. The technique is compared to Stokes parameter analysis [8] of the polarimetric response as well as to a novel differential interferometric polarimetry technique which utilises phase changes between two polarimetry states to contrast the object. Results for these techniques are presented initially for B-scan GPR images. The paper also describes the polarisation channel equalisation and quasi-bistatic antenna calibration procedure undertaken to acquire more accurate imagery. The paper is organised as follows. Section II outlines the measurement environment and

section III explains the calibration routine for the quasi-bistatic setup. The full polarimetric clutter suppression technique is described in IV and the Stokes parameters are applied to the same dataset and compared in section V. Section VI introduces a new differential interferometric polarimetry discrimination technique that is again applied to the same data. Finally, Section VII gives an engineering assessment of the results.

II. MEASUREMENT SYSTEM & EXPERIMENTAL METHODOLOGY

A. System and Antennas

The stepped frequency radar is built around a Rhode & Schwarz ZVA 10675E vector network analyser that acts as the coherent transmitter-receiver unit. The other parts of the system are the transmitting and the receiving antenna and the computer to perform the signal processing. The experimental setup is shown in Figure 1. The presented GPR system uses a linear polarised TEM horn as transmit antenna and two near-field probe (loop) antennas, arranged orthogonally and in front of the TEM horn, to collect the co- and cross-polar response. The loop antennas are placed just outside the near-field of the TEM horn at 12cm in front of the aperture at 400 MHz. The antenna array is scanned over a 3m sandpit automatically under computer control.

B. Experimental Setup

Experiments have been conducted on the indoors soil facility which consists of one soil bay (2.4Lx1.2Wx0.8H meters) filled with sand; and one bay (1.2Lx1.2Wx0.8H meters) filled with RAM for placing calibration targets, such as a 40 mm sphere for co-polar calibration and a brass rod, placed in an 22.5° angle perpendicular to the direction of antenna movement, for cross-polar calibration. The soil is maintained within a 1-3% moisture content and at a constant temperature of 25°C . A Near-Field Measurement System (NFMS) has been erected over the two bays with a 3m long linear automated positioner. The antenna array acquires the scattering parameter S_{21} across the 0.4-4.8 GHz frequency spectrum and takes measurements at 1cm intervals along the horizontal x-axis. Figure 1 shows the dual polarised near-field antenna configuration. The setup uses a linear polarised TEM (Scientific Atlanta) horn that illuminates

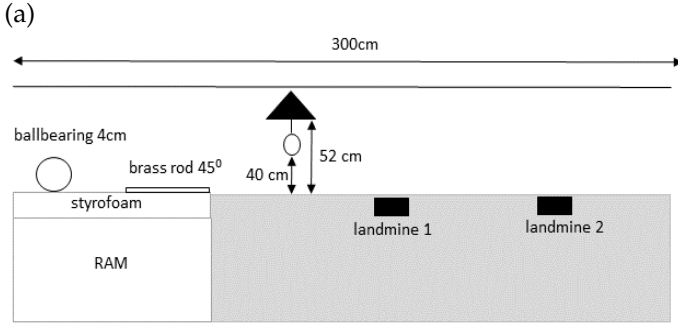
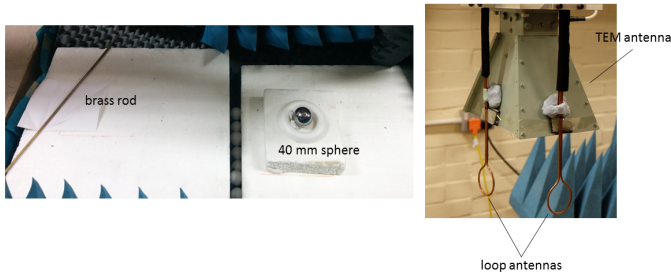


Figure 1: Calibration targets and antenna head (a), sketch of measurement setup (b), laboratory scene (c).

the ground scene in vertical (V) polarisation. The local back-scattered electromagnetic field is collected by two loop antennas arranged orthogonally and in front of the TEM antenna to acquire VV and VH (vertical-horizontal) co- and cross-polarised data. The loop antennas are 40cm above the soil surface. The antenna height is typical of a stand-off GPR. This height is a trade-off between such factors as the energy attenuation, decreasing the antenna-soil coupling, avoiding possible obstacles of the ground surface, and forming sufficient antenna footprint for future SAR processing. To make orthogonal polarization measurements, i.e. HH and HV, the antenna array is rotated clockwise by 90° [11] and data taken.

C. Signal Analysis

The complex S -parameter measurements are converted to range profiles. The VNA uses a Stepped Frequency Continuous Waveform (SFCW) consisting of N pulses, equally separated by Δf Hertz. The phase of the sampled quadrature mixer output is,

$$\phi_n = -2\pi(f_0 + n\Delta f)\frac{2z}{c} \quad (1)$$

where z is the range to the object and f_0 is the frequency of the first transmitted pulse [12] may be expressed as the complex spectral return S of amplitude A_n as,

$$S(f_n) = A_n \exp(j\phi_n). \quad (2)$$

The N complex samples in each burst are Inverse Fast Fourier Transformed (IFFT) to a series of complex range reflectivity profiles. It can be shown that taking the IFFT (or FFT) of M samples (from N pulses) corresponding to a range bin divides the range bin into finer subdivisions resulting in a smoother range profile [13]. In this experiment a total of $N = 801$ sample steps were taken in each measurement and resampled to $M = 4096$. B-scans for VV, HH and HV polarization can be seen in Figure 2-4.

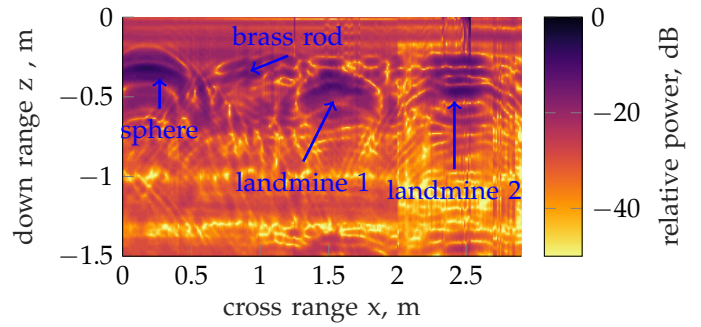


Figure 2: VV polarisation B-scan image of the radar scene with targets indicated.

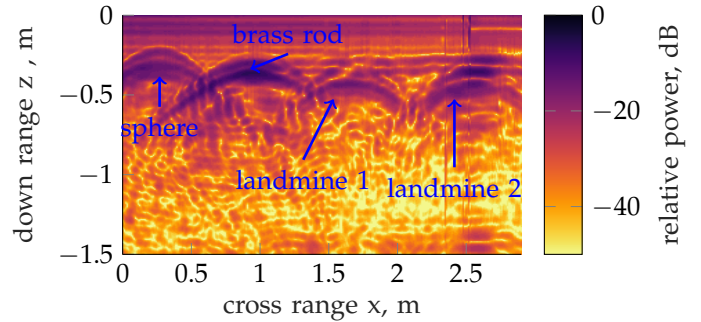


Figure 3: HH polarisation B-scan image of the radar scene with targets indicated.

Figures 2 and 3 show, that all targets are present in co-polar channels, i.e. HH and VV. As expected, the calibration sphere is missing in cross-polar HV (Figure 3) and the landmines are present. Moreover, in all images significant subsurface clutter is present. This is due artefacts from processing as well as physical clutter being present. Therefore, we now investigate techniques to reduce the subsurface clutter in the images.

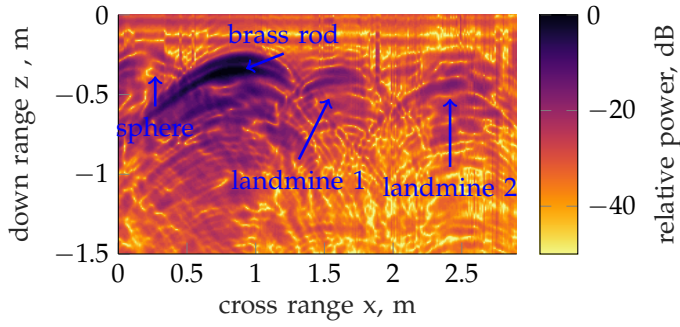


Figure 4: HV polarisation B-scan image of the radar scene with targets indicated.

III. CHANNEL CALIBRATION

Since, receive and transmit antennas are different, the system is bistatic. Although the radar polarimetry is derived from the monostatic case and the antennas are located very close to each other, calibration of the system is crucial [6]. The scattering matrix $S_{bistatic}$, equation (3), obtained by the measurement system is different from the one of the monostatic case. To accommodate and calibrate the phase to mimic the monostatic system response, we used an extrapolation method. Figure 5 shows the calibration scheme, viewed from the top of the antennas. The calibration object, in this case the rod, stays static at one position, as does the transmit antenna, and the receive antenna is moved N positions away from the rod. Measurements are taken in 1cm increments. In this case we moved the antenna head $N = 20$ positions. The plots for difference in phase and difference in amplitude for each polarization at each position are shown in Figure 6 and 7, respectively. Calculation of the correction factor $\overline{\psi}_{nm}$ is shown in equations (4) and (5). The phase and amplitude, at each position $N > 1$ is subtracted from the phase or amplitude at position $N=1$ and the result plotted. The phases and amplitudes are extrapolated to position zero (i.e. ideal monostatic positions) and averaged. This is done for each polarization and polarization matrix is formed. Each pixel in each polarization B-scan is multiplied with this correction factor.

$$S_{bistatic} = \begin{bmatrix} S_{11} & S_{12} \\ S_{21} & S_{22} \end{bmatrix} \quad (3)$$

$$\psi_{nm} = A_c(\cos(\Phi_c) + j\sin(\Phi_c)) \quad (4)$$

$$\overline{\psi}_{nm} = \left(\sum_{n=1}^N \psi_{nm} \right) / N \quad (5)$$

$$S_{monostatic} = \begin{bmatrix} S_{11}\overline{\psi}_{11} & S_{12}\overline{\psi}_{12} \\ S_{21}\overline{\psi}_{21} & S_{22}\overline{\psi}_{22} \end{bmatrix} \quad (6)$$

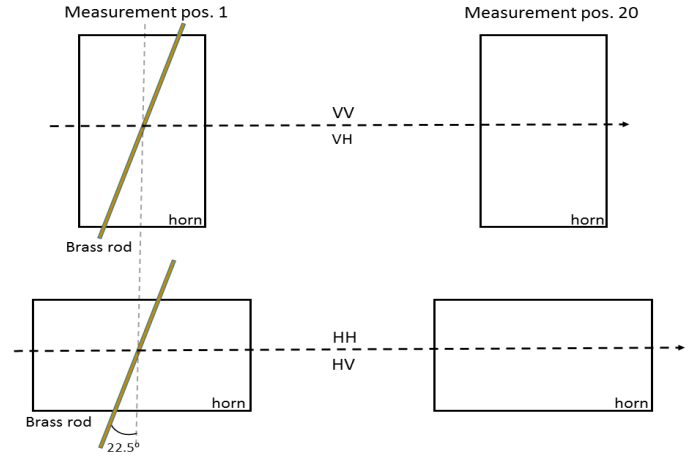


Figure 5: Schematic diagram illustrating the polarimetric correction calibration procedure.

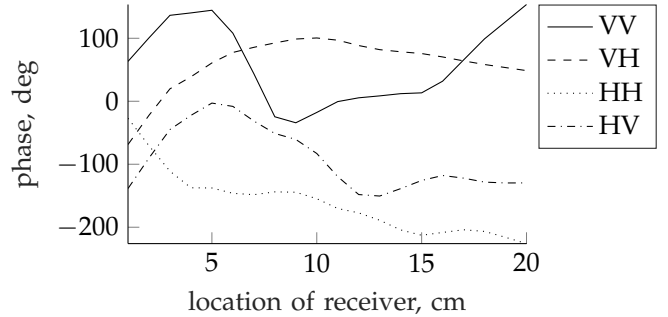


Figure 6: Difference in Phase of 20 increments away from calibration target Φ_c .

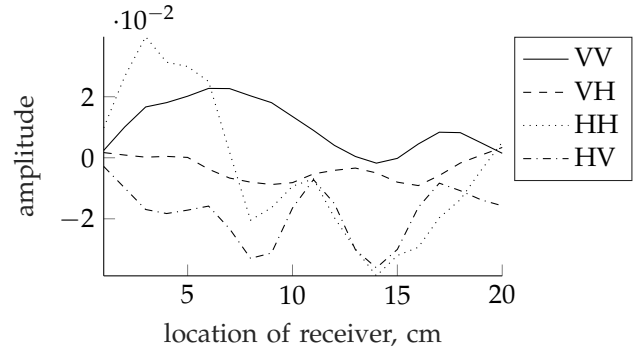


Figure 7: Difference in amplitude of 20 increments away from calibration target A_c .

IV. YAMAGUCHI POLARIMETRY DECOMPOSITION

In [7] Moriyama demonstrates it is possible to synthesize a radar channel at any polarisation state from the scattering matrix. If E_t is the transmitted wave and E_s the scattered wave from the target then E_t can be defined by the Jones matrix as,

$$E_t = \frac{1}{\sqrt{1 + \rho\rho^*}} \begin{bmatrix} 1 \\ \rho \end{bmatrix}. \quad (7)$$

where ρ is the polarisation ratio. The scattered wave is related to the transmitted wave via the scattering matrix where $S[HV]$ represents the targets polarimetric scattering characteristics in the HV basis. The co-polar and cross-polar powers can then be obtained. The co-polar power,

$$P_{co} = |E_t^T(HV) \cdot S[HV] \cdot E_t(HV)|^2 \quad (8)$$

where T denotes the transpose and \perp denotes the orthogonal polarisation. The complex null polarisation value is calculated from the appropriate polarimetric co- and cross-polar power expression by setting it to zero and solving for the roots of the matrix as given by [7],

$$\rho_{co,null} = \frac{S_{HV} \pm \sqrt{S_{HV}^2 - S_{HH} \cdot S_{VV}}}{S_{VV}} \quad (9)$$

and co-polar power is

$$P_x = \left| \frac{S_{HH} + 2 \cdot S_{HV}\rho + S_{VV} \cdot \rho^2}{1 + \rho\rho^*} \right|^2 \quad (10)$$

In the case of cross-polar power E_t case the transmitted is again defined by the Jones scattering matrix as,

$$E_{\perp,t} = \frac{1}{\sqrt{1 + \rho\rho^*}} \begin{bmatrix} \rho^* \\ -1 \end{bmatrix} \quad (11)$$

and the cross-polar power is deduced as,

$$P_x = |E_{\perp,t}^T(HV) \cdot S[HV] \cdot E_t(HV)|^2 \quad (12)$$

and the roots are again found by setting equation (12) to zero

$$\rho_{x,null} = \frac{-B \pm \sqrt{B^2 - 4AC}}{2A} \quad (13)$$

where,

$$A = S_{HH}^* S_{HV} + S_{HV}^* S_{VV} \quad (14)$$

$$B = |S_{HH}|^2 - |S_{VV}|^2 \quad (15)$$

$$C = -A^* \quad (16)$$

$$P_x = \left| \frac{S_{HH}\rho^* + S_{HV}(\rho\rho^* - 1) - S_{VV}\rho}{1 + \rho\rho^*} \right|^2 \quad (17)$$

The polarimetric clutter matrix, is agnostic in the sense that it does not know the type of clutter we wish filtering e.g. it could be antenna coupling, or as here, subsurface clutter in the sand. Once the clutter region is selected the polarimetric pixels are extracted to form the clutter matrix, S_{sand} .

$$S_{sand} = \begin{bmatrix} 1.430 + 1.437j & 0.150 - 0.150j \\ 0.150 - 0.150j & 1.352 - 0.661j \end{bmatrix} \cdot 10^{-2} \quad (18)$$

There are two possible roots to Equation (13) for the sand co-polar scattering matrix polarisation given below,

$$\rho_{co,1} = -0.7133 \cdot 10^{-2} + 0.4566j \quad (19)$$

$$\rho_{co,2} = -0.7133 \cdot 10^{-2} - 0.4566j. \quad (20)$$

Taking ρ value from equation (19) the co-polar channel power can be calculated. A similar procedure is repeated for the P_x case and the results for the co- and cross-polar power responses are shown in Figure 8. The B-scans show significantly reduced clutter levels in both co- and cross-polar filters. The response from the brass rod has been reinforced as anticipated and the sphere response weakened due to its lack of cross-polar signals. The trihedral and landmine are well contrasted, in both, co- and cross-polar.

V. STOKES PARAMETERS

The polarisation state of a plane wave can be characterised by the Stokes parameters. Only three of these Stokes parameters are independent, they are related by the complex field vectors:

$$I_0^2 = Q^2 + U^2 + V^2 \quad (21)$$

This relation only holds true if the wave is fully polarized and can thus be used as an indicator of the quality of polarization in our experiment.

$$I_0 = E_V E_V^* + E_H E_H^* \quad (22)$$

$$Q = E_V E_V^* - E_H E_H^* \quad (23)$$

$$U = E_V E_H^* + E_H E_V^* \quad (24)$$

$$V = j(E_V E_H^* - E_H E_V^*) \quad (25)$$

The Stokes vector representation I_0 and Q can be used to display the individual intensities of the horizontal and vertical polarization:

$$I_v = |E_v|^2 = (I_0 + Q)/2 \quad (26)$$

$$I_h = |E_h|^2 = (I_0 - Q)/2 \quad (27)$$

I_0 represents the total intensity of a wave, Q represents the difference between vertically and horizontally polarized intensities and U and V represent jointly the phase difference between the vertically and horizontally polarised components of the wave. All four Stokes parameters have been computed to study if they can be used as means of clutter suppression. The summation of horizontal and vertical intensities (I_0) and the difference

between horizontal and vertical intensities (Q), as well as the individual intensities of vertical (I_v) and horizontal (I_h) polarizations can be seen in Figure 9. Analysis of the results indicate that the Stokes parameters do show all targets and clutter is significantly reduced, as is the power of the targets. Interestingly, the butterfly landmine, which is a low contrast target, is visible.

VI. DIFFERENTIAL INTERFEROMETRIC POLARIMETRY

Differential Interferometric Polarimetry (DinPol) takes advantage of phase changes between two polarimetry states in this case HH and VV. Equation, (28) and (29) illustrate the technique. The authors previously applied this [14] to exploit phase contrast in single polarimetry imagery of drying soil around a buried object, here by combining the phase contrast in the appropriate Stokes parameters we can expose and localise different scattering mechanisms. Therefore,

$$P(x, y) = \sum_{n=1}^{pol_{state}} \Delta\phi(x, y)_n \cdot |p(x, y)_n| \quad (28)$$

where,

$$\Delta\phi(x, y)_n = \angle \left(\frac{p(x, y)_{n+1}}{|p(x, y)_{n+1}|} \cdot \frac{|p(x, y)_n|}{p(x, y)_n} \right) \quad (29)$$

where the summed $P(x, y)$ pixel is the magnitude weighted differential phase contrast of the complex valued $p(x, y)$ pixel at position (x, y) of the individual B-scans that compose either co- or cross-polar images. DinPol has much reduced clutter levels of similar magnitude to Stokes, but the image contrast appears to be not as effective as Yamaguchi imagery.

The resultant images are shown in Figure 10 for co-polar (VV, HH) and cross-polar (VH, HV) DinPol. The images retain all the polarimetric scattering mechanism of Stokes parameters while suppressing random clutter. Hence the DinPol co-polar almost completely suppressed the air-ground interface and retains targets with single or odd bounce scattering features; on the other hand, the DinPol cross-polar retains only objects with diplane scattering with relative orientation of 45° . It was anticipated that no subsurface objects would be present, however, a partial scatter from the brass rod calibration object is present. This was found experimentally to originate from a slight dip on the brass rod in the horizontal plane.

VII. DISCUSSION AND SUMMARY CONCLUSIONS

An experimental set-up for performing GPR measurements and test signal-processing and imaging algorithms has been developed. This experimental set-up composes one sand bay to bury targets and one bay filled with RAM to place calibration targets such as a 40mm sphere and a brass rod on. Landmines from different shapes and materials have been measured and channel balancing

and novel bistatic calibration has been performed on the measured dataset. Various Stokes and Yamaguchi polarimetric decompositions were investigated to provide clutter suppression on data collected for shallow buried butterfly and shoebox landmines in sand. It was shown, that the air-ground-interface and the antenna cross talk can effectively be suppressed in Yamaguchi co- and cross-polar products while the various scattering mechanisms can be localised and clutter suppressed using Stokes parameters. Moreover, a novel DinPol decomposition technique was also applied and observed to provide complementary interpretation of subsurface scattering mechanisms. Taken together these techniques provide significant performance enhancements at least in subsurface image contrast. Further work is undergoing to design techniques to quantify the image improvements and clutter reduction performance.

VIII. ACKNOWLEDGMENT

The authors thank the Find A Better Way charity for their support of this research under the DETERMINE programme (grant number 2015/001D).

REFERENCES

- [1] D.J. Daniels *Ground Penetrating Radar*, 2nd ed. London, England: IET, 2007.
- [2] H. Jing and T. Vladimirova, *Novel algorithm for landmine detection using C-scan ground penetrating radar signals*, Seventh International Conference on Emerging Security Technologies (EST), Canterbury, 2017, pp. 68-73.
- [3] S. Sarjoghian and Y. Alfadhl and X. Chen *Compact ultra-wideband double-ridged horn antennas for medical imaging*, 2016 Loughborough Antennas Propagation Conference (LAPC), 2016 .
- [4] K. V. Hoel and S. Kristoffersen and J. Moen and G. Holm and T. S. Lande *Characterization of a 3D printed wideband waveguide and horn antenna structure embedded in a UAV wing*, 2016 10th European Conference on Antennas and Propagation (EuCAP), 2016.
- [5] W. S. Benedix et al. *External calibration of GPR antenna accommodated on a rover*, Proceedings of the Fourth European Conference on Antennas and Propagation, 2010.
- [6] Y. Yamaguchi, T.Nishikawa, M. Sengoku, W.-M. Boerner, H.J. EOM, *Fundamental Study on Synthetic Aperture FM-CW Radar Polarimetry*, IEICE Transactions on Communications Vol. E77-B No.1, Jan. 1994.
- [7] T. Moriyama, H. Kasahara, Y. Yamaguchi, H. Yamada *Advanced Polarimetric Subsurface FM-CW Radar*, IEEE Transactions on Geoscience and Remote Sensing, 1998.
- [8] F.T. Ulaby, C. Elachi, *Radar Polarimetry for Geoscience Applications*, Norwood, MA: Artech House, 1990.
- [9] R. McGrath *Legacy of Conflict: a Manual for Development Workers*, Diane Publishing Company, 1998.
- [10] E.Banks, *Brassey's Essential Guide To Anti-Personnel Landmines, Recognizing and Disarming*, Potomac Books Inc; 1st English ed edition, 1998, ISBN 1-85753-228-7.
- [11] I.L. Morrow, S. Wirth, M. Finnis *Discrimination of Buried Objects using Time-Frequency Analysis and Waveform Norms*, LAPC 2016.
- [12] M. Skolnik, *Radar Handbook - 2nd Edition*, McGraw-Hill, 1990, ISBN 0-07-057913-X.
- [13] D. R. Wehner. *High Resolution Radar*. Artech House, Chap. 5, second edition, 1995.
- [14] S.G. Wirth, I.L. Morrow, D. Andre *Microwave Phase Contrast Imaging of the Subsurface using Variation in Soil Moisture Level*, IEEE MTT-S International Conference on Numerical Electromagnetic and Multiphysics Modeling and Optimization (NEMO), Aug. 2018, Reykjavik, Iceland, pp. 978-1-5386-5204-61.

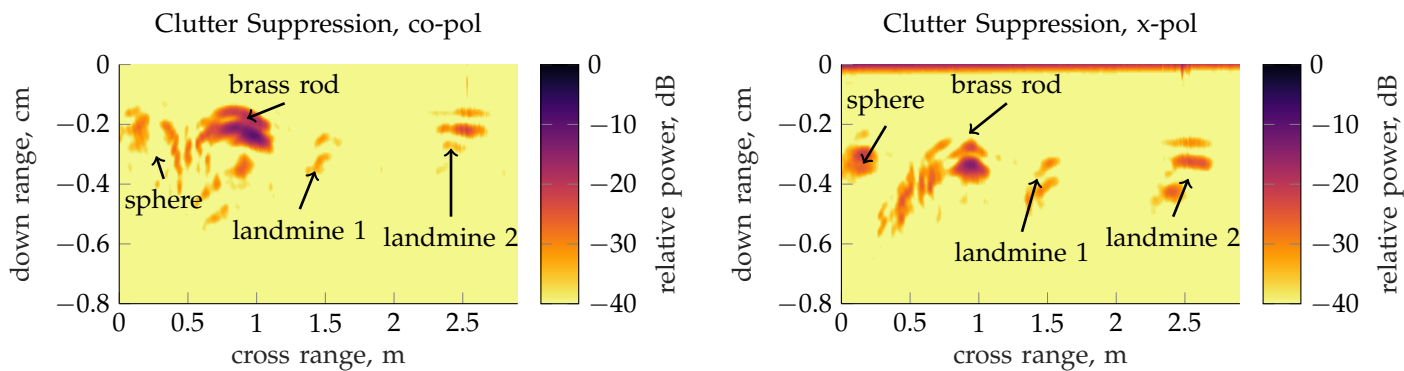


Figure 8: Co- and cross-polar polarimetric clutter suppression.

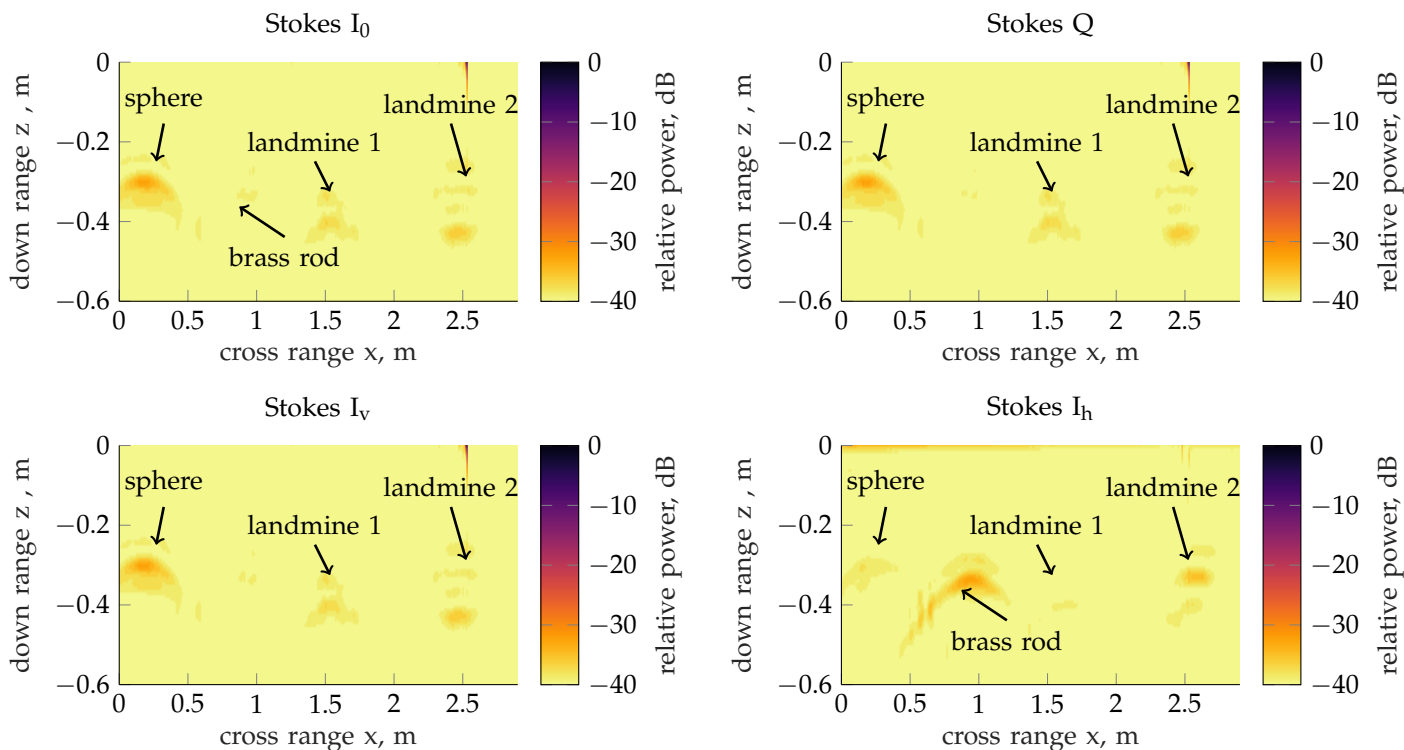


Figure 9: Top: Stokes parameters I_0 and Q , Bottom: I_v and I_h .

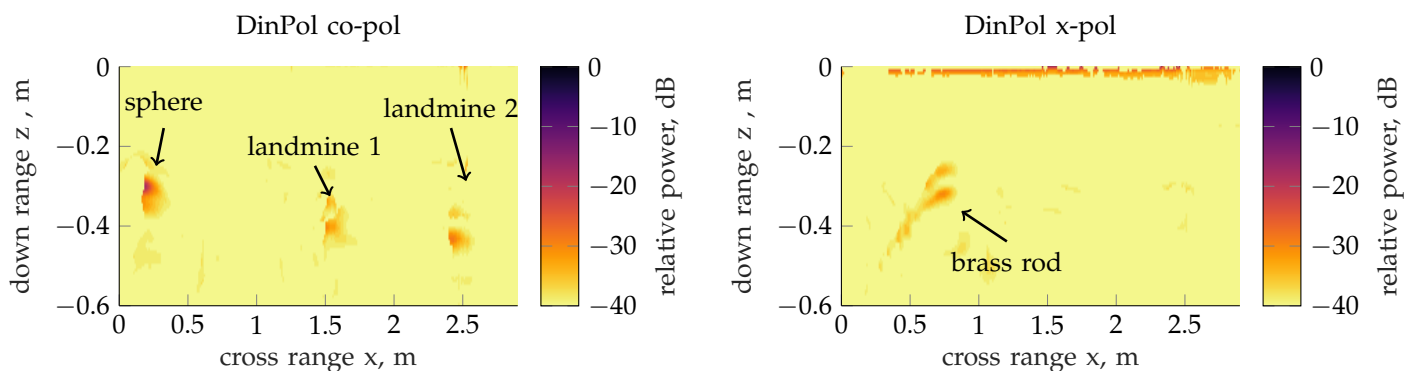


Figure 10: Co- and cross-polar DinPol results.

Effective polarization filtering techniques for ground penetrating radar applications

Morrow, Ivor L.

2019-01-10

Attribution-NonCommercial 4.0 International

Wirth S & Morrow IL (2019) Effective polarization filtering techniques for ground penetrating radar applications. In: AMTA (Antenna Measurement Techniques Association Symposium) 2018, Williamsburg, VA USA, 4-9 November 2018.

<https://ieeexplore.ieee.org/document/8604167>

Downloaded from CERES Research Repository, Cranfield University